Active tension and membrane friction mediate cortical flows and blebbing in a model actomyosin cortex

R. Sakamoto [1,2] and M. P. Murrell [1,2,3,*]

[1]*Department of Biomedical Engineering, Yale University, 10 Hillhouse Avenue, New Haven, Connecticut 06520, USA*
[2]*Systems Biology Institute, 850 West Campus Drive, West Haven, Connecticut 06516, USA*
[3]*Department of Physics, Yale University, 217 Prospect Street, New Haven, Connecticut 06511, USA*

(Received 23 April 2024; accepted 12 June 2024; published 3 July 2024)

Blebs, spherical membrane bulges of the cell membrane, are ubiquitous structures observed in various biological phenomena, including apoptosis, cell division, to bleb-based cell migration. The mechanics of blebbing have been characterized in terms of the actin cytoskeleton beneath the cell membrane. However, how changes in cortical mechanics relate to changes in the physical behaviors of the cell remains unclear. Here, we reconstitute a minimal model of the actomyosin cortex within liposomes. Upon laser ablation of the cortex, myosin-induced mechanical stresses are relaxed by different mechanisms—either cortical flows or membrane blebbing. For cortical flows, the cortex-membrane composite behaves as a viscoelastic fluid. By contrast, for ablation-induced blebbing, elastic stresses are accumulated, and the cortex behaves as a solid with a stress yield. These results highlight pivotal roles for membrane elasticity, cytoskeleton, and pressure in the mechanical responses of the actomyosin cortex.

DOI: 10.1103/PhysRevResearch.6.033024

I. INTRODUCTION

Blebbing, an outward spherical protrusion of cell plasma membrane, is a ubiquitous phenomenon observed in apoptosis [1], cell division [2,3], and bleb-based cell migration [4–7]. The actin cytoskeleton comprises actin filaments (F-actin) and myosin II motors, driving various morphological changes of cells from division to migration by transmitting contractile forces to the plasma membranes through actin-membrane links [8,9]. Blebs play pivotal roles in achieving many biological functions, such as releasing intracellular pressure to stabilize cell shape symmetry during division [10], and directional guidance during cell migration by finding least friction pores under confined environments such as extracellular matrices [11,12]. The mechanism of blebbing has been well documented in terms of the mechanics of the actin cytoskeleton beneath the cell plasma membrane: the actin cortex detaches from the membrane or is dissociated, creating a hole, generating a pressure gradient across the membrane to drive outward membrane protrusion [13–16]. Recent experimental studies suggested that the expansion of the bleb membrane introduces the Ca^{2+} into the cytosol through activating ion channels, suggesting that membrane mechanics may also play a vital role in regulating ion channel function [17].

Although the formation process of blebbing has been well characterized, how different cortical and membrane behaviors emerge is not well understood. For example, laser ablation techniques, in which high-power lasers locally dissociate the cortex, have been used as useful tools to probe cortex mechanics [18]. Ablation of a single rounded cell cortex induces local blebbing [15], while laser ablation can also induce cortical flows [19]. Thus, it remains elusive what mechanical parameters determine the diverse responses of the cortex and membrane upon external mechanical stimuli. To address this, we developed a biomimetic model of cell blebbing comprising actomyosin networks encapsulated within giant unilamellar vesicles (liposomes) [20–29]. Here, we employed laser ablation of the actin cortex along with light-activated actomyosin contractility, enabling precise control of mechanical responses. The laser ablation induces diverse responses, including cortical actomyosin flow and membrane blebbing. Combining experiments with physical modeling, we identified that active tension and friction between the cortex and the membrane determine the dynamics and propensity for flowing and blebbing. This study elucidates the interplay between myosin-induced active tension, the mechanical properties of the actin network, and membrane shape changes, providing insights into the coordination between cytoskeletal forces and membrane mechanics in cells.

*Contact author: michael.murrell@yale.edu

II. RESULTS

A. Laser ablation induces various morphological responses

Purified actin, myosin, and actin-associated proteins were encapsulated into liposomes using the inverted emulsion method (Methods) [20,27,30]. His-tagged VCA is anchored

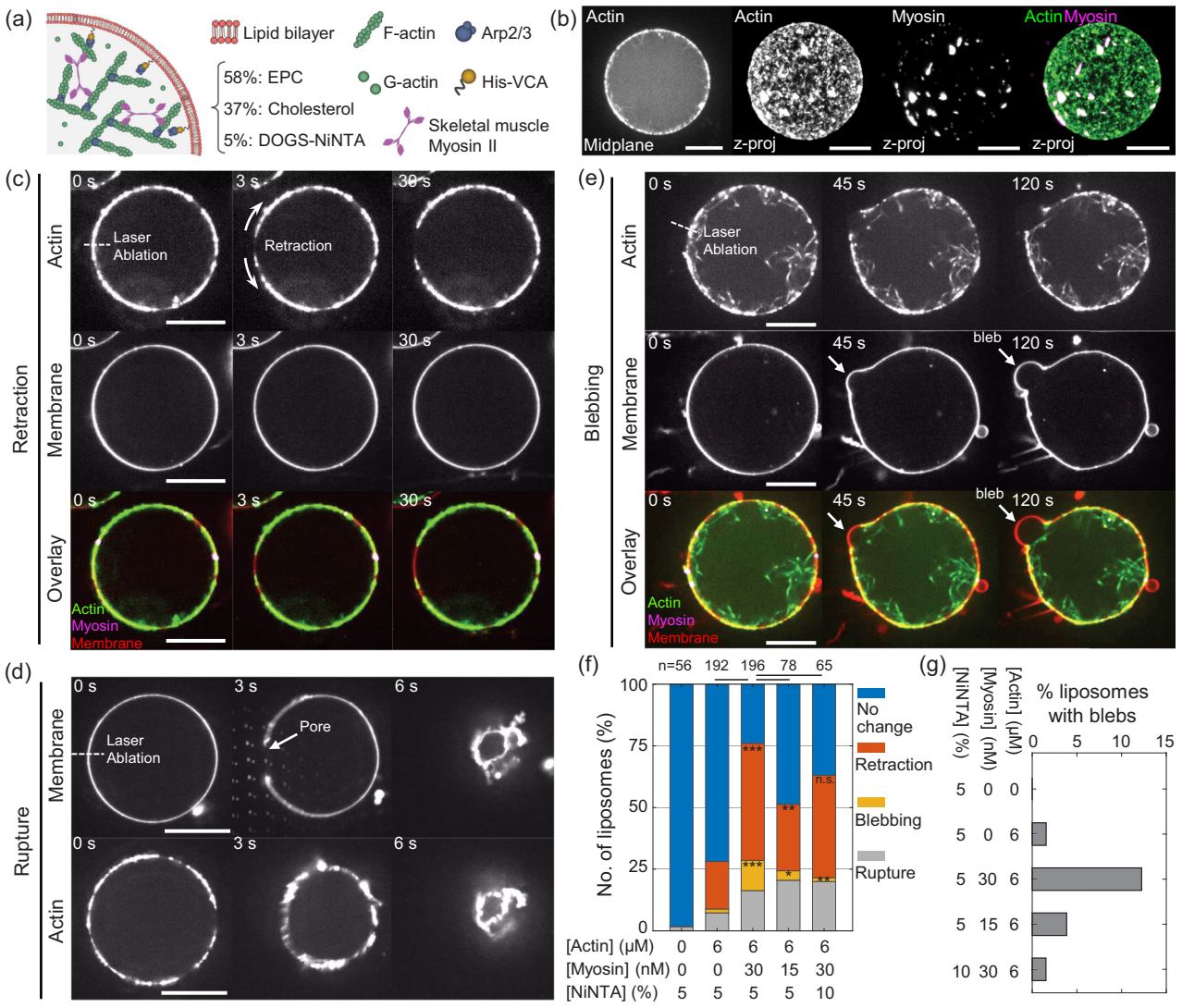

FIG. 1. Morphological changes of the actomyosin cortex liposomes upon laser ablation. (a) Schematic of a liposome encapsulating actomyosin and actin-associated proteins. A branched actin network is polymerized by the Arp2/3 complex via His-VCA-mediated activation. (b) Snapshots showing midplane and z projection of an actomyosin cortex liposome (actin in green, myosin in magenta). (c)–(e) Time-lapse images showing morphological responses of actomyosin cortex liposomes upon laser ablation exhibiting retraction (c), rupture (d), and blebbing (e) (actin in green, myosin in magenta, and membrane in red). (f) Percentage of liposomes showing no change (blue), retraction (orange), blebbing (yellow), and rupture (gray) upon ablation. n is the total number of liposomes ($N = 3$ independent experiments in [actin] $= 6\,\mu$M, [myosin] $= 0$ nM, [NiNTA] $= 5\%$; $N = 13$ in [actin] $= 6\,\mu$M, [myosin] $= 0$ nM, [NiNTA] $= 5\%$; $N = 18$ in [actin] $= 6\,\mu$M, [myosin] $= 30$ nM, [NiNTA] $= 5\%$; $N = 6$ in [actin] $= 6\,\mu$M, [myosin] $= 15$ nM, [NiNTA] $= 5\%$; $N = 4$ in [actin] $= 6\,\mu$M, [myosin] $= 30$ nM, [NiNTA] $= 10\%$). Top lines denote p values comparing morphological responses between two conditions. (g) Percentage of liposomes with blebs in different conditions. *, **, *** stand for $p < 0.05$, $p < 0.01$, $p < 0.001$, respectively. n.s.: not significant. Scale bars, 10 μm.

to the membrane via DOGS-NiNTA lipids, polymerizing the actin cortex beneath the membrane through the activation of the Arp2/3 complex [Figs. 1(a) and 1(b)]. These liposomes are referred to as actomyosin cortex liposomes. Gelsolin and cofilin were included to maintain the dynamics of F-actin assembly and disassembly [20,27,30]. Myosin was initially inactivated by adding blebbistatin, an inhibitor of myosin ATPase activity [31], before the preparation of liposomes to allow the formation of the actomyosin cortex without inducing contraction. The liposomes were then illuminated with 488 nm light to inactivate blebbistatin before the laser ablation [27,32,33]. Light-activated actomyosin contractility was confirmed by observing the contraction of actin networks polymerized within the liposome volume that does not contain His-VCA and Arp2/3 (Supplemental Material Fig. 1 [34]).

To probe the mechanical properties of the actomyosin cortex, we performed laser ablation of the actomyosin cortex, a method previously established in cells [15,19]. We ablate the actomyosin cortex using an N_2 pulsed dye laser ($\lambda = 435$ nm, 26 μJ). Notably, we observed three distinct morphological responses immediately after local ablation: retraction of the actomyosin cortex from the ablated area [Fig. 1(c) and Supplemental Material Movie S1 [34]], rupturing of the liposome [Fig. 1(d) and Supplemental Material Movie S2 [34]],

and blebbing of the membrane [Fig. 1(e) and Supplemental Material Movie S3 [34]]. Specifically, 48% of liposomes exhibited retraction of the actomyosin cortex without generating blebs, while 13% displayed the growth of cell-like blebs, 16% ruptured, and 23% showed no change [Fig. 1(f)].

B. Characterization of blebbing behavior

Blebbing was characterized by an outward bulge of the membrane protruding from the opened-up actomyosin cortex, reminiscent of "blebs" observed in cells [Fig. 1(e) and Supplemental Material Fig. 2 [34]). Blebs exhibited a spherical shape protruding from the surface of the mother liposomes, where the bleb diameter $D_B = 3.7 \pm 2.3\,\mu m$ (mean +/− standard deviation; $n = 27$) was always smaller than the mother liposome diameter $D_{ML} = 21.8 \pm 5.3\,\mu m$. Some mother liposomes exhibited slight deviations from a spherical shape during bleb expansion (Supplemental Material Fig. 2 [34]). Notably, when a second ablation is performed at the opposite side of the first bleb, the height of the second bleb was approximately two to three times smaller than the first bleb (Supplemental Material Fig. 3 [34]). This observation supports a pressure-driven mechanism for cell-like bleb formation, where the first bleb relaxes the accumulated pressure, thereby the second bleb becomes smaller [15].

We compare the probability of bleb formation upon laser ablation among different myosin concentrations and NiNTA lipid fractions [Fig. 1(f)]. The blebbing probability increased from 1.6% at [myosin] = 0 nM to 13% at [myosin] = 30 nM [Fig. 1(g)]. However, it decreased from 13% to 4% when the myosin concentration was reduced from 30 to 15 nM, indicating the contribution of actomyosin contractility to the generation of blebs [Fig. 1(g)]. The small fraction of actin cortex liposomes at [myosin] = 0 nM exhibiting a bleb-like structure may be attributed to stress built up by actin polymerization [35]. More than 95% of bare liposomes lacking actin and myosin exhibited no morphological changes upon laser ablation. In contrast, the probability of rupture increased at actomyosin cortex liposomes (20%) and actin cortex liposomes lacking myosin (15%). This observation suggests the potential contribution of the actin cortex to liposome rupturing.

A large fraction of actomyosin cortex liposomes (47%) exhibited cortical retraction, whereas the probability of retraction decreased in actin cortex liposomes (19%) [Fig. 1(f)]. We confirmed the effect of reduced myosin concentration by observing a reduction in the number of myosin puncta incorporated within a liposome (Supplemental Material Fig. 4 [34]). Moreover, increasing the NiNTA lipid fraction from 5% to 10% reduced the blebbing probability from 12% to 2% [Fig. 1(g)], indicating that stronger membrane-to-cortex attachment may prevent bleb formation, as observed in cells [36]. We confirmed the influence of a higher NiNTA lipid fraction through the observation that 10% NiNTA lipid fraction leads to higher actin fluorescence at the cortex compared to 5% NiNTA lipid fraction. This indicates that the higher NiNTA lipid fraction enhanced the localization of His-VCA, thereby enhancing actin polymerization beneath the membrane (Supplemental Material Figs. 5 and 6 [34]).

C. Cortical retraction is controlled by myosin concentration and membrane-to-cortex attachment

First, we analyze the cortical retraction dynamics to estimate the mechanical parameters of the actomyosin cortex. The arc length of the opened-up region upon ablation is defined as L, and the retraction speed is defined as v_{ret} [Fig. 2(a)]. Notably, both the maximum arc length L_{max} and initial retraction speed v_0 significantly increased with higher myosin concentration, changing from $v_0 = 0.12 \pm 0.09$ to $v_0 = 0.52 \pm 0.32$ $\mu m\,s^{-1}$, confirming the contribution of actomyosin contractility to cortical retraction [Figs. 2(b)–2(e)]. Of note, the cortical retraction speed is comparable to the reported myosin puncta walking speed $v_{myo} \sim 0.1$–$1.0\ \mu m\,s^{-1}$ within the F-actin network nucleated by the Arp2/3 complex on a two-dimensional lipid bilayer [37,38].

On the other hand, increasing the membrane-to-cortex attachment by using the larger fraction of NiNTA lipids resulted in slower cortical retraction $v_0 = 0.22 \pm 0.10\ \mu m\,s^{-1}$ at [NiNTA] = 10% compared to $v_0 = 0.52 \pm 0.32\ \mu m\,s^{-1}$ at [NiNTA] = 5% (Supplemental Material Fig. 7 [34]), indicating that the strength of the physical link between the cortex and membrane determines the cortical retraction speed through the friction between the cortex and membrane [21]. We confirmed that there is no significant liposome size dependence on the retraction speed and arc length (Supplemental Material Fig. 7 [34]). It is worth noting that the contraction of Arp2/3 networks was minimal in two-dimensional systems, consistent with the result that the typical arc length in the present system is typically less than 10% of the circumference length of the liposome [37]. Together, these results suggest that actomyosin contractility and the membrane-to-cortex attachment determine the mechanical response upon laser ablation.

D. Active tension and cortex-membrane friction determine cortical retraction dynamics

To understand how changes in the mechanical properties of the cortex lead to changes in cortical retraction behavior, we employed the Kelvin-Voigt (KV) model, incorporating an active component as used in previous studies [18,19,39]. The membrane acts as a damper, while actomyosin serves as an active elastic component connected in parallel, describing the elastic response upon sudden stress release via ablation [Fig. 3(a)]. The dynamics of retraction induced by laser ablation is described by $\zeta dL/dt = -kL - \gamma_a + \gamma_0$, where L is the arc length, γ_a is the active tension due to actomyosin contractility within the cortex, ζ is the frictional damping coefficient due to the interaction between the cortex and membrane which absorbed the cortex thickness for dimensional correctness, k is the stiffness of the cortex, and γ_0 is the mechanical tension present in the system before ablation [19,21,39]. Upon ablation, $\gamma_0 = 0$, and the cortical retraction proceeds until the system reaches a mechanical equilibrium. Analysis of the KV model gives the retraction speed as a function of time t after ablation, $v_{ret}(t) = v_0 \exp(-t/\tau)$, where $v_0 = \gamma_a/\zeta$ is the initial retraction speed and $\tau = \zeta/k$ is the characteristic retraction time [Figs. 3(b)–3(e)]. Thus, the KV model relates the mechanical parameters of the actomyosin cortex to experimentally measurable quantities.

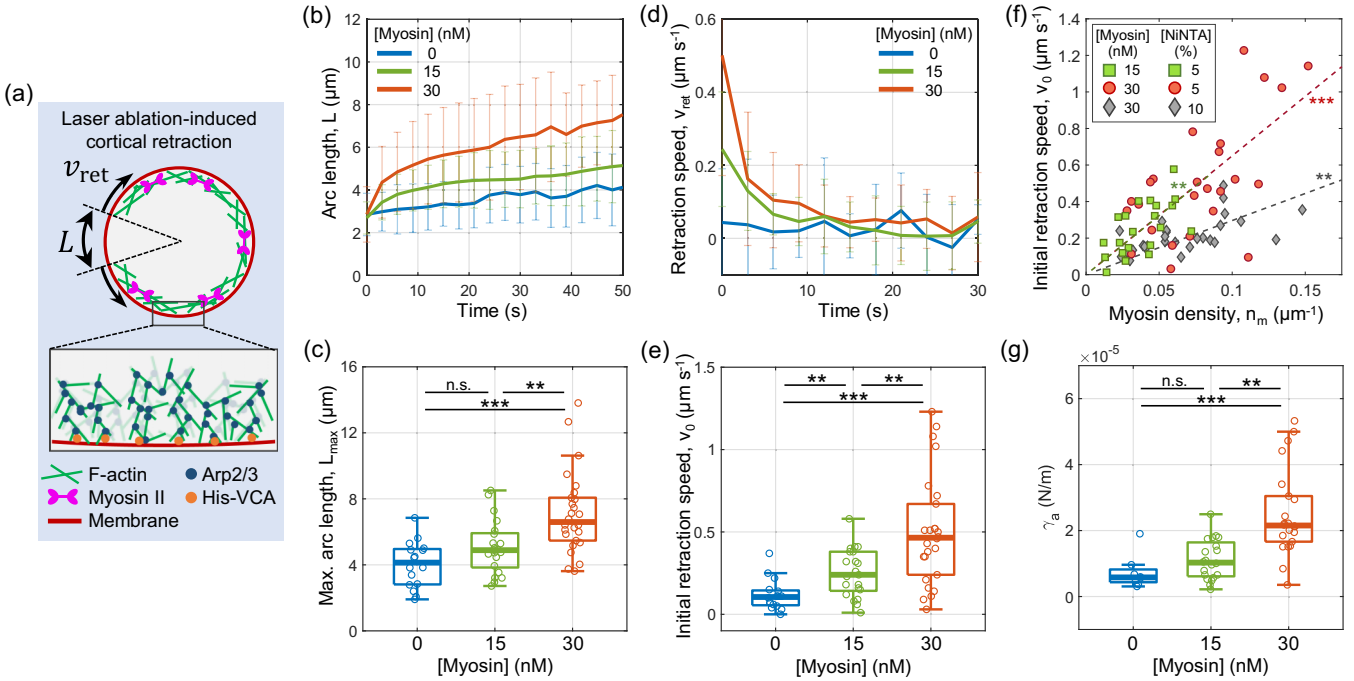

FIG. 2. Cortical retraction is controlled through actomyosin contractility. (a) Schematic depicting cortical retraction, defining arc length L, and retraction speed $v_{\rm ret}$. (b) and (c) Arc length over time (b) and maximum arc length $L_{\rm max}$ boxplots (c) with varying myosin concentrations ($n = 16$ actomyosin cortex liposomes and $N = 4$ independent experiments at [myosin] = 0 nM; $n = 21$ and $N = 4$ at [myosin] = 15 nM; $n = 26$ and $N = 5$ at [myosin] = 30 nM). Time = 0 s corresponds to 3 s after laser ablation. (d) and (e) Retraction speed $v_{\rm ret}$ over time (d) and initial retraction speed v_0 boxplots (e). (f) Initial retraction speed v_0 dependence on myosin puncta density n_m within liposomes, varying myosin concentration and NiNTA fraction ($N = 4$ at [myosin] = 30 nM, [NiNTA] = 10%). Broken lines are linear regression $v_0 = (\alpha/\zeta)n_m$, with $(\alpha/\zeta) = 6.46$ at [myosin] = 15 nM, [NiNTA] = 5%; $(\alpha/\zeta) = 6.50$ at [myosin] = 30 nM, [NiNTA] = 5%; and $(\alpha/\zeta) = 2.96$ at [myosin] = 30 nM, [NiNTA] = 10%. (g) Boxplot showing active tension γ_a obtained from the Kelvin-Voigt model. Curves and error bars are mean ± standard deviation. **, *** stand for $p < 0.01$, $p < 0.001$, respectively. n.s.: not significant.

First, we test the model prediction that the initial retraction speed v_0 is determined by the active tension γ_a and the friction between the cortex and membrane ζ, following the relation $v_0 = \gamma_a/\zeta$. We assumed that the active tension γ_a is proportional to the myosin puncta density: $\gamma_a = \alpha n_m$, where α is a proportionality coefficient independent of myosin density [39–41]. Thus, the initial retraction speed is proportional to the myosin density: $v_0 = (\alpha/\zeta)n_m$, which was used to fit the experimental data to extract mechanical parameters [Fig. 2(f)]. The slope of the $v_0 - n_m$ relation is $(\alpha/\zeta) = 6.46$ at [myosin] = 15 nM, which is comparable to $(\alpha/\zeta) = 6.50$ at [myosin] = 30 nM [Fig. 2(f)]. Therefore, we estimate the ratio of the active tension to be $\gamma_a^{\text{Myo 30 nM}}/\gamma_a^{\text{Myo 15 nM}} = \zeta v_0^{\text{Myo 30 nM}}/(\zeta v_0^{\text{Myo 15 nM}}) \simeq v_0^{\text{Myo 30 nM}}/v_0^{\text{Myo 15 nM}} \simeq 2.0$ [Fig. 2(e)], consistent with the ratio of the active tension estimated from myosin density, $\gamma_a^{\text{Myo 30 nM}}/\gamma_a^{\text{Myo 15 nM}} = \alpha n_m^{\text{Myo 30 nM}}/(\alpha n_m^{\text{Myo 15 nM}}) = n_m^{\text{Myo 30 nM}}/n_m^{\text{Myo 15 nM}} \simeq 2.1$ (Supplemental Material Fig. 4 [34]). This theoretical analysis suggests that the faster retraction speed at higher myosin concentrations is induced by the higher active tension (i.e., contractility) within the actomyosin cortex.

On the other hand, the linear relationship between v_0 and n_m was also observed under the condition of stronger membrane-to-cortex attachment at [NiNTA] = 10% [Fig. 2(f)]. Thus, the theoretical relationship $v_0 = (\alpha/\zeta)n_m$ holds in this condition. However, the slope of the $v_0 - n_m$ relation is $(\alpha/\zeta) = 2.96$ at [NiNTA] = 10%, which is 2.2 times smaller than the slope $(\alpha/\zeta) = 6.50$ at [NiNTA] = 5% [Fig. 2(f)]. Assuming that the proportionality coefficient α is independent of membrane-to-cortex attachment, we estimate the ratio of the friction between the cortex and membrane to be $\zeta^{10\%\ \text{NiNTA}}/\zeta^{5\%\ \text{NiNTA}} \sim 2.2$. Therefore, this theoretical analysis suggests that the stronger membrane-to-cortex attachment causes larger friction between the cortex and membrane during cortical retraction. Moreover, the characteristic retraction time τ was obtained by fitting $v_{\rm ret}(t)$ to the time course of the retraction speed by varying v_0 and τ [Figs. 3(b)–3(e)]. The characteristic retraction time $\tau = 12.0 \pm 6.3$ s at [NiNTA] = 10% was longer than that of $\tau = 5.5 \pm 6.0$ s at [NiNTA] = 5%, indicating that the larger friction due to stronger membrane-to-cortex attachment delayed the retraction. Together, the theoretical analysis using the KV model provides a mechanical understanding that actomyosin contractility and friction via membrane-to-cortex attachment determine the dynamics of cortical retraction upon laser ablation.

It should be noted that the proportionality coefficient α introduced in $\gamma_a = \alpha n_m$ could take larger values at stronger membrane-to-cortex attachment, because myosin II under higher load is known to perform larger mechanical work [42–44]. However, the larger α indicates a steeper slope of the $v_0 - n_m$ relation, which contradicts the experimental observation of the smaller slope at stronger membrane-to-cortex attachment. Hence, we concluded that the myosin load

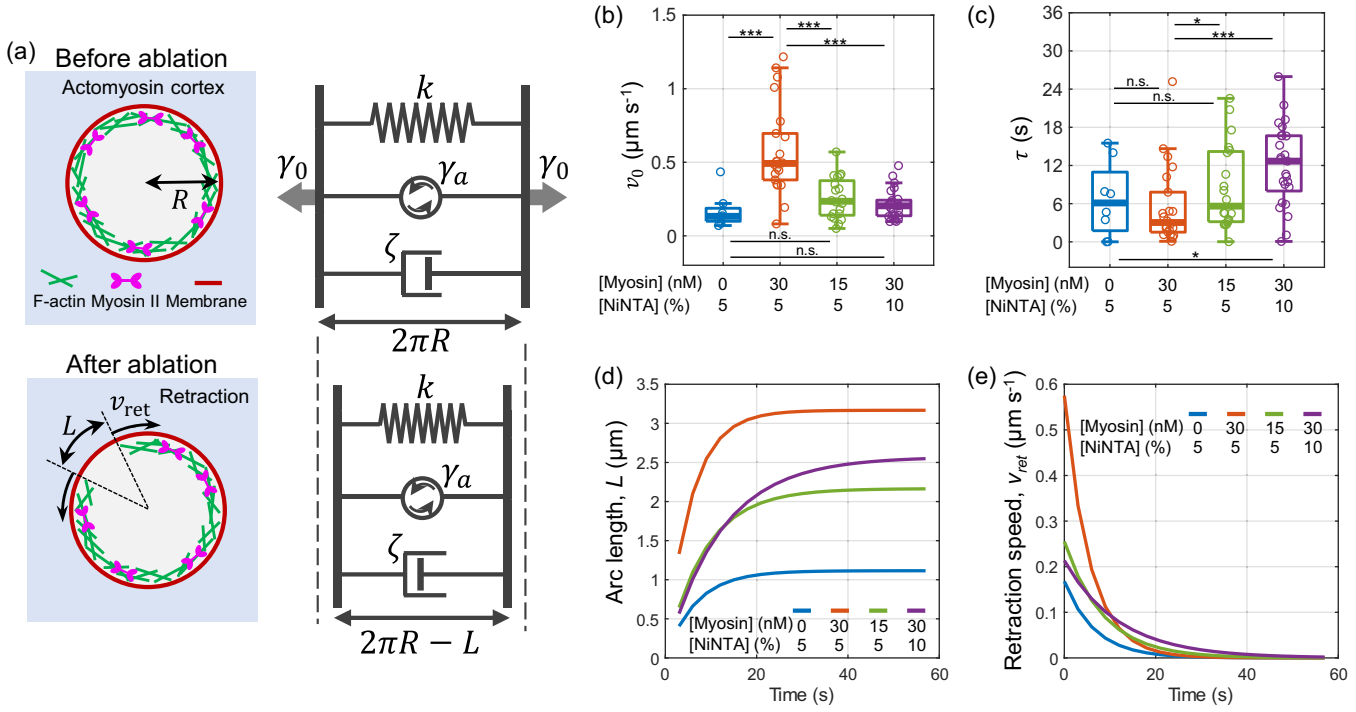

FIG. 3. Kelvin-Voigt model of the laser ablation-induced cortical retraction. (a) Schematic showing the KV model parameters, active tension γ_a, friction between the cortex and the membrane ζ, elasticity of the cortex k, and γ_0 is the mechanical tension present in the system before ablation. Upon ablation, $\gamma_0 = 0$, and the cortical retraction proceeds until the system reaches a mechanical equilibrium. (b) and (c) Initial retraction speed, $v_0 \equiv \gamma_a/\zeta$ (b), and characteristic retraction timescales, $\tau \equiv \zeta/k$ (c), were obtained by fitting the experimental data of retraction speed to $v_{\rm ret}(t) = v_0 \exp(-t/\tau)$ ($n = 8$ liposomes, $N = 4$ independent experiments in [myosin] = 0 nM, [NiNTA] = 5%; $n = 22$, $N = 5$ in [myosin] = 30 nM, [NiNTA] = 5%; $n = 20$, $N = 4$ in [myosin] = 15 nM, [NiNTA] = 5%; $n = 25$, $N = 4$ in [myosin] = 30 nM, [NiNTA] = 10%). (d) and (e) Theoretical curves of the arc length (d) and retraction speed (e) plotted using the mean values of v_0 and τ obtained from the experimental data. *, **, *** stand for $p < 0.05$, $p < 0.01$, $p < 0.001$, respectively. n.s.: not significant.

dependence is not significant in the present system and the influence of the larger friction ζ outweighed the myosin load dependence.

E. Estimation of the cortex tension during cortical retraction

We next estimated the mechanical parameters of the actomyosin cortex. During cortical retraction, the retracting cortex experiences the friction force by the lipid bilayer membrane. The friction force per unit area applied to the gel by the membrane is given by $f_{\rm fric} = \zeta' v_{\rm ret} = \eta_m n_{\rm link} v_{\rm ret}$ [21], where η_m is the membrane viscosity, typically on the order of 10^{-6}–10^{-5} Pa s m [21,26,30], and $n_{\rm link}$ is the number density of membrane-to-cortex links, estimated as follows. Assuming all the Arp2/3 complex is bound to the membrane-bound VCA sites and Arp2/3 concentration of 0.3 μM, for an actomyosin cortex liposome with a radius $R = 10\,\mu$m, the total number of membrane-to-cortex links is $N_{\rm link} \sim 10^5$, calculated by multiplying the Arp2/3 concentration and the volume of the liposome [21,26]. We ignored the viscous resistance of the actin network ($\sim \eta_c v_{\rm ret} R^{-2}$) as it is expected to be orders of magnitude smaller than the friction force, given the two-dimensional viscosity of actin $\eta_c = \eta h \sim 10^{-9}$–$10^{-6}$ Pa s m, where the actin viscosity $\eta \sim 10^{-2}$–10^{1} Pa s [30,45] and the cortex thickness $h = 0.31 \pm 0.13\,\mu$m (Supplemental Material Fig. 5 [34]), assuming Arp2/3 does not affect the gel viscosity [46]. Using the relationships $v_0 = \gamma_a/\zeta$ and $\gamma_a = h\sigma_a$ [34,47], where σ_a is active stress, the initial force balance is written as $(\zeta/h)v_0 = \sigma_a$. Comparing this with the friction force, the frictional coefficient is written as $\zeta = \eta_m n_{\rm link} h$. Using $\eta_m n_{\rm link} = \eta_m N_{\rm link}/(4\pi R^2)$, the cortex thickness $h = 0.31 \pm 0.13\,\mu$m (Supplemental Material Fig. 5 [34]), and the initial retraction speed $v_0 = 0.52 \pm 0.32\ \mu$m s^{-1}, the active tension γ_a is estimated as $\gamma_a = \zeta v_0 = (\eta_m n_{\rm link} h) v_0$, yielding $\gamma_a \sim 10^{-6}$–10^{-5} N m^{-1} [Fig. 2(g)]. This value is comparable to the active tension estimated from the number of myosin puncta within an actomyosin cortex liposome (Supplemental Material Fig. 4 [34]) [27], and the reported actomyosin cortical tension estimated for cell-sized liposomes [21].

The estimated active tension is one order of magnitude larger than the membrane tension of the bare liposomes $\gamma_m = (5.8 \pm 8.1) \times 10^{-7}$ N m^{-1} measured by membrane fluctuation spectroscopy (Supplemental Material Fig. 8 [34]). This result confirms that our theoretical estimates are based on the "active" contribution that outweighs the "passive" membrane tension. Indeed, thermal fluctuation of the membrane was suppressed upon polymerization of the actin cortex (Supplemental Material Fig. 8 [34]). The membrane tension of the bare liposomes behaves like liquid surface (interfacial) tension, which is related to the Laplace's pressure through $\Delta P = 2\gamma_m/R$ [48]. It should be noted that there is a minimal retraction speed at [myosin] = 0 nM, even though the model assumes active tension as a source of retraction after ablation.

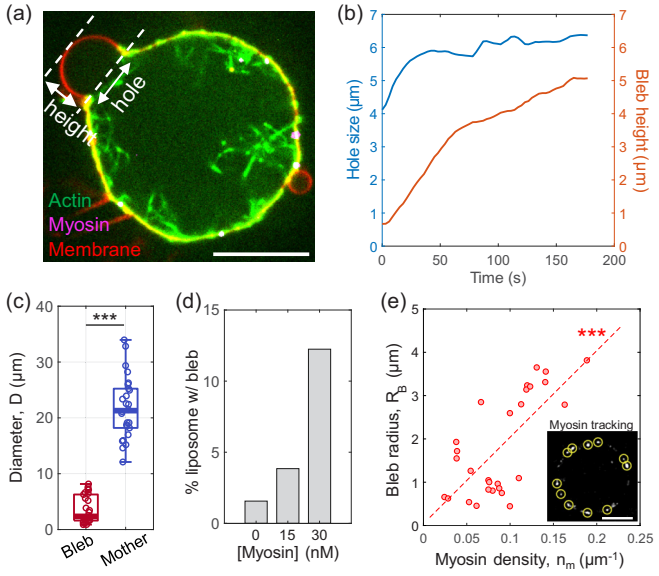

FIG. 4. Laser ablation-induced blebbing is driven by actomyosin contractility. (a) Snapshot of a laser ablation-induced bleb in an actomyosin cortex liposome (actin in green, myosin in magenta, and membrane in red). (b) Time course of the hole size and bleb height of the liposome in (a). (c) Boxplot comparing bleb and mother liposome diameters ($n = 27$, $N = 16$). (d) Liposome blebbing fractions upon laser ablation at different myosin concentrations ($n = 78$, $N = 6$ at [myosin] = 0 nM; $n = 192$, $N = 13$ at [myosin] = 15 nM; $n = 196$, $N = 18$ at [myosin] = 30 nM). (e) Bleb size dependence on myosin puncta density n_m within a liposome ($n = 27, N = 16$). Inset: myosin spot tracking (yellow circles). Scale bars, 10 μm. *, **, *** stand for $p < 0.05$, $p < 0.01$, $p < 0.001$, respectively. n.s.: not significant.

We hypothesize such a slight opening without myosin may be due to a loss of adhesion between the cortex and the membrane. As shown in the fluctuation spectroscopy analysis (Supplemental Material Fig. 8 [34]), membrane fluctuation is suppressed upon polymerization of the cortical actin layer, which suggests an increase in tension. Upon ablation, there is a difference in the extent of adhesion between the regions covered with the actin cortex and without the actin cortex in the vicinity of the ablated area. This gradient in adhesion strength may induce a slight opening. Nevertheless, the initial retraction speed with myosin is significantly faster than without myosin, highlighting the important contribution of myosin to retraction. The estimated active tension at [myosin] = 0 nM is comparable to the tension $\gamma_m = (2.2 \pm 2.0) \times 10^{-6}$ N m^{-1} of the actin cortex liposome measured by fluctuation spectroscopy (Supplemental Material Fig. 8 [34]), which may be attributed to the tension built up by actin polymerization [35]. Together, the theoretical estimation further supports that cortical retraction is driven by actomyosin contractility.

F. Blebbing is controlled through actomyosin cortex tension

We next investigate the impact of cytoskeletal mechanics on blebbing. Upon laser ablation, bleb expansion is accompanied by the increase in bleb height and hole size [Figs. 4(a) and 4(b), and Supplemental Material Fig. 2 [34]). The bleb diameter $D_B = 3.7 \pm 2.3$ μm was consistently smaller than that of the mother liposome $D_{ML} = 21.8 \pm 5.3$ μm [Fig. 4(c)]. The frequency of blebbing increased with the concentration of myosin [Fig. 4(d)], and the size of the blebs increased with a higher number density of myosin puncta [Fig. 4(e)], indicating that actomyosin contractility is crucial to generate blebs.

To understand how actomyosin contractility leads to blebbing, we estimate the active tension required for bleb expansion [13–15,49]. The Young-Laplace law in the mother liposome is written as $\Delta P = 2(\gamma_a + \gamma_m)/R_{ML}$, where γ_a and γ_m is the active tension and the membrane tension, respectively. γ_a vanishes in the region where the actomyosin cortex is disrupted by the laser ablation, leading to the outgrowth of the bleb. The maximal pressure in the bleb has previously been expressed as $\Delta P = 4\gamma_m/w$, where w is the width of the laser-ablated region of the cortex [15,49]. Below this pressure, membrane tension limits bleb expansion, while above it, expansion proceeds until reaching mechanical equilibrium [15]. Thus, the active tension for bleb expansion is estimated by the balance between the pressure inside the mother liposome and the pressure in the bleb, yielding the active tension $\gamma_a \sim \gamma_m R_{ML}/w \sim 10^{-6}$ N m^{-1}, using the membrane tension of a bare liposome measured by fluctuation spectroscopy $\gamma_m = (5.8 \pm 8.1) \times 10^{-7}$ N m^{-1} (Supplemental Material Fig. 8 [34]), $R_{ML} = 10$ μm, and $w = 1$ μm. The estimated active tension γ_a is comparable to the active tension estimated from the cortical retraction [Fig. 2(g)], and the active tension estimated from the number of myosin puncta within a liposome, $\gamma_a \sim (1.1 \times 10^{-6})$–$(8.3 \times 10^{-6})$ N m^{-1} [Fig. 3(d) and Supplemental Material Fig. 4 [34]] [27].

III. DISCUSSION

We developed a biomimetic model cortex exhibiting various cell-like morphological behaviors, including cortical retraction, blebbing, and rupture. Combining laser ablation of the cortex and physical modeling, we determined that myosin-based active tension and actin-membrane friction are key factors governing cortical retraction and blebbing. Myosin-induced mechanical stresses relax through two pathways upon laser ablation: either through cortical retraction or blebbing. In the case of cortical retraction, the active tension balanced within the cortex was disrupted by ablation and dissipated through actin-membrane friction during retraction, until the active tension balances with the elastic stresses that build up during retraction. In blebbing, the active tension balanced within the cortex was disrupted by ablation, leading to membrane expansion, until the active tension balances the elastic stresses built up due to the shrinkage of the cortex surface area. These distinct pathways of the cortical responses, involving either retraction [19] or blebbing [15] in response to external mechanical stimuli, may be regulated in cells depending on cellular states and desired cellular functions. Together, this study established a mechanical link between cytoskeletal-generated stresses and membrane dynamics.

The cortex tension in the present study system was one to two orders of magnitude smaller than in cells [15], likely due to the less defined actin-membrane attachment, lower myosin concentration, differences in myosin properties, and contributions from other sources (e.g., ion channels). For comparison, based on the estimate of a 43 800 nonmuscle myosin IIA (NMIIA) clusters participating in the retrograde flow of

U2OS cell lamellipodia [50], and each detectable myosin cluster likely containing a minimum of approximately one to ten myosin filaments [51], along with the typical volume of a U2OS cell being ∼4000 μm^3 [52,53], we estimate the active NMIIA concentration in a cell to be ∼20–200 nM. Future studies would be necessary to employ cellular actin-membrane linkers such as ezrin [54], and NMIIA as in cells that presumably generates higher stress with a more significant load-dependent duty ratio [55].

One could imagine a transition behavior between retraction or blebbing, depending on the system parameters, such as active tension or myosin concentration. We observed that bleb size increases with the number of myosin puncta (Fig. 4), implying a continuous transition from retraction to blebbing. However, precise control of the number of myosin molecules in a liposome is challenging, limiting our capability to quantitatively characterize the transition behavior. Investigating the transition between retraction and blebbing remains an important future challenge. Additionally, 23% of liposomes did not exhibit either retractions or blebbing at [myosin] = 30 nM (Fig. 1), likely because the number of myosin incorporated in liposomes was not sufficiently large, limiting successful outcomes. We display all results from the laser ablation experiment to clarify experimental reproducibility. Future studies will focus on improving encapsulation methods and maintaining myosin activity to increase reproducibility and achieve well-controlled actomyosin contraction, further characterizing blebbing and retraction behavior.

While the mechanism determining whether retraction or blebbing occurs remains unclear, we suggest that the heterogeneity of the actin cortex may differentiate between them: a well-defined, uniform cortex generates pressure effectively, leading to blebbing, whereas a heterogeneous cortex is ineffective in generating pressure, resulting in retraction within the cortex (Supplemental Material Fig. 9 [34]). A more profound understanding of the diverse mechanical responses of the actomyosin cortex would be further studied by utilizing the present experimental system, together with theoretical modeling encompassing the coupled mechanics of the actomyosin cortex and membrane dynamics [56,57].

IV. METHODS

A. Lipid compositions

Liposomes are formed with a combination of L-α-phosphatidylcholine from egg yolk (Egg phosphatidylcholine (EPC), 840051C, 58%), cholesterol (ovine wool, 110796, 36%), and 1,2-dioleoyl-sn-glycero-3-[n(5-amino-1-carboxypentyl) iminodiacetic acid]succinyl nickel salt (DOGS-NTA-Ni, 5%). Lipids were purchased from Avanti Polar Lipids (Alabaster, AL). For fluorescent contrast, we use Oregon Green 1,2-dihexadecanoyl-sn-glycero-3-phosphoethanolamine (O12650; Invitrogen) at 1% or 23-(dipyrrometheneboron difluoride)-24-norcholesterol (TopFluor Cholesterol; 810255; Avanti) at 1%.

B. Preparation of liposomes

Liposomes were prepared by following the previously published methods [27,30]. First, lipids in chloroform are combined in a glass vial and dried under Ar gas. The chloroform is dried, and the lipids are dissolved in mineral oil (Sigma-Aldrich) at 2 mg/ml. The oil mixture is then sonicated in a bath sonicator for 2 h at room temperature. The mixture is stored at 4 °C for up to 1 week. Then 7 µl of final buffer (FB) is added to 70 µl of mineral oil in a 0.65-ml tube (07200185; Corning Costar). This mixture is then syringed in a glass syringe (Hamilton) one to two times and the tube is placed on ice for 15 min. Separately, in a low absorption 0.65-ml tube, 30 µl of mineral oil is added to the top of 30 µl of outer buffer (OB). Then, the 60-µl emulsion is added to the top of the mineral oil layer in the tube. This mixture is then centrifuged at 100 g for 15 min at 4 °C.

C. Buffers

Buffers are prepared by following the previously published methods [27,30]. Briefly, myosin storage buffer (MSB) contains 0.5 M KCl, 0.1 M HEPES (N-2-hydroxyethylpiperazine-N-2-ethane sulfonic acid), and skeletal muscle myosin (rabbit, MY02; Cytoskeleton Inc.) is 10 µM. This is the buffer myosin is stored in as dimer, after it has been fluorescently labeled. The spin-down buffer (SDB) contains 2 µl dark phalloidin, 4.2 µl of 238 µM actin, 40 µl internal polymerization (IP) buffer, 20 µl myosin (in MSB), and 4.3 µl of 4.6 M KCl. Spun at 39 000 rpm for 1 h at 4 °C. The IP buffer contains 3.2 mM $CaCl_2$, 3.2 mM $MgCl_2$, 8 mM HEPES, 0.8 mM DTT, 0.4 mM DABCO, 8 mM ATP, 50 mg/ml dextran, 175 mM sucrose, 0.1 mg/ml glucose oxidase, 0.04 mg/ml catalase, 0.5% glucose to minimize photobleaching. Protein mix (PM): Protein is added at the following concentrations: 6.3 µM nonfluorescent actin (AKL99-D; Cytoskeleton Inc.), 0.7 µM rhodamine-actin (AR05-C; Cytoskeleton Inc.), 1.5 µM VCA-his (1:10 VCA), 0.3 µM Arp2/3 (RP01P-B; Cytoskeleton Inc.), 60 nM gelsolin (HPG6-A; Cytoskeleton Inc.), and 70 nM cofilin (CF01-C; Cytoskeleton Inc.). Blebbistatin (1 µl of 0.8 M) was added to keep the myosin inactive until imaged. Internal, nonpolymerizing buffer (INP buffer) contains 0.1 mM $CaCl_2$, 10 mM HEPES, 6 mM DTT, 0.13 µM DABCO, 140 mM sucrose, 50 mg/ml dextran, and 0.2 mM ATP. The OB contains 10 mM HEPES (pH 7.5), 2 mM $MgCl_2$, 0.2 mM $CaCl_2$, 2 mM ATP, 6 mM DTT, 0.13 mM DABCO, 390 mM glucose, and 0.01 mg/ml casein. The FB contains 4 µl INP, 3.25 µl PM, 13.3 µl IP, and 2 µl SDB buffer supernatant. The final KCl concentration was kept at 50 mM by adding an additional amount according to the myosin concentration. This is the buffer that will encapsulate within the liposome using the inverted emulsion method. The FB is approximately 355 mOsm. The osmolarity of the OB is adjusted with glucose such that the osmotic pressure difference between the OB and the FB is between 20 and 60 mOsm. All the reagents were purchased from Sigma-Aldrich.

D. Protein concentrations

The final concentration of nonfluorescent actin (AKL99-D; Cytoskeleton Inc.), rhodamine-actin (AR05-C; Cytoskeleton Inc.), and myosin within the liposomes is 6.3 µM, 0.7 µM, and 0–30 nM, respectively. VCA was used at 1.5 µM. Arp2/3 (RP01P-B; Cytoskeleton Inc.) for actin polymerization was at 0.3 µM. Gelsolin (HPG6-A; Cytoskeleton Inc.) and cofilin

(CF01-C; Cytoskeleton Inc.) severing proteins were at 60 and 70 nM, respectively. Details of the buffer conditions, protein purification, and labeling procedures are available in Supplemental Material Note 1 [34].

E. Ablation experiments

The ablation is done using the Micropoint laser setup. The dye laser (435 nm; Andor Technology) ablates a line shape with 5 μm in length to cut the actin cortex. A 60× oil-immersion objective (Leica Microsystems) was used for ablation and the laser power was held at 65% (26 μJ). The imaging protocol was set to have three frames of $dt = 3$ s preablation and $dt = 3$ s postablation.

F. Microscopy

Images were acquired by a Leica DMi8 inverted microscope equipped with a 63×1.4 numerical aperture oil-immersion lens (Leica Microsystems), a spinning-disk confocal microscope (CSU22; Yokagawa), and a sCMOS camera (Zyla; Andor Technology) controlled by Andor iQ3 (Andor Technology).

G. Image analysis

Quantitative image analysis was performed by using a custom code written in MATLAB. The fluorescence intensity of the membrane was detected through the binarization of fluorescence images after applying a median filter to remove the shot noise in the images taken by the confocal microscope. The liposome and bleb radius R were estimated from the projection assumed to be πR^2. Myosin spot tracking was performed by using the Fiji plugin MOSAICSUITE particle tracker 2D.

H. Statistical analysis

Statistical tests comparing distributions are done with the Wilcoxon rank sum test. Statistical tests comparing bar plots are done with Fisher's exact test. All data displayed as a single value with an error bar is quoting the mean +/− standard deviation. The symbols *, **, and *** represent $p < 0.05$, 0.01, and 0.001, respectively. Fitted lines are shown to reject the null hypothesis to an extent that depends on the quoted p value.

The data supporting this manuscript are available from the contact author upon request.

ACKNOWLEDGMENTS

The authors acknowledge funding under Grant No. ARO MURI W911NF-14-1-0403, Grant No. NIH RO1 GM126256 (to M.P.M.), Grant No. NIH U54 CA209992 (to M.P.M), Human Frontier Science Program (HFSP) Grant No. RGY0073/2018 (to M.P.M), and Yale startup funding. R.S. acknowledges support from the Overseas Postdoctoral Fellowships of the Uehara Memorial Foundation, Overseas Fellowship of Japan Society for the Promotion of Science (JSPS), and Yale startup funding.

R.S. and M.P.M. designed the experimental work. R.S. acquired the experimental data. R.S. contributed new reagents and analytic tools. R.S. analyzed experimental data. R.S. drafted the paper. R.S. and M.P.M. edited the paper.

Any opinion, findings, and conclusions or recommendations expressed in this material are those of the authors and do not necessarily reflect the views of the NSF, NIH, ARO, HFSP, Uehara Memorial Foundation, or JSPS.

The authors declare no competing interests.

[1] M. L. Coleman, E. A. Sahai, M. Yeo, M. Bosch, A. Dewar, and M. F. Olson, Membrane blebbing during apoptosis results from caspase-mediated activation of ROCK I, Nat. Cell Biol. **3**, 339 (2001).

[2] E. Boucrot and T. Kirchhausen, Endosomal recycling controls plasma membrane area during mitosis, Proc. Natl. Acad. Sci. USA **104**, 7939 (2007).

[3] N. Taneja and D. T. Burnette, Myosin IIA drives membrane bleb retraction, Mol. Biol. Cell **30**, 1051 (2019).

[4] Y. J. Liu, M. Le Berre, F. Lautenschlaeger, P. Maiuri, A. Callan-Jones, M. Heuze, T. Takaki, R. Voituriez, and M. Piel, Confinement and low adhesion induce fast amoeboid migration of slow mesenchymal cells, Cell **160**, 659 (2015).

[5] M. Bergert, A. Erzberger, R. A. Desai, I. M. Aspalter, A. C. Oates, G. Charras, G. Salbreux, and E. K. Paluch, Force transmission during adhesion-independent migration, Nat. Cell Biol. **17**, 524 (2015).

[6] V. Ruprecht, S. Wieser, A. Callan-Jones, M. Smutny, H. Morita, K. Sako, V. Barone, M. Ritsch-Marte, M. Sixt, R. Voituriez, and C. P. Heisenberg, Cortical contractility triggers a stochastic switch to fast amoeboid cell motility, Cell **160**, 673 (2015).

[7] H. Blaser, M. Reichman-Fried, I. Castanon, K. Dumstrei, F. L. Marlow, K. Kawakami, L. Solnica-Krezel, C. P. Heisenberg, and E. Raz, Migration of zebrafish primordial germ cells: A role for myosin contraction and cytoplasmic flow, Dev. Cell **11**, 613 (2006).

[8] G. Salbreux, G. Charras, and E. Paluch, Actin cortex mechanics and cellular morphogenesis, Trends Cell Biol. **22**, 536 (2012).

[9] M. Murrell, P. W. Oakes, M. Lenz, and M. L. Gardel, Forcing cells into shape: The mechanics of actomyosin contractility, Nat. Rev. Mol. Cell Biol. **16**, 486 (2015).

[10] J. Sedzinski, M. Biro, A. Oswald, J. Y. Tinevez, G. Salbreux, and E. Paluch, Polar actomyosin contractility destabilizes the position of the cytokinetic furrow, Nature (London) **476**, 462 (2011).

[11] K. M. Yamada and M. Sixt, Mechanisms of 3D cell migration, Nat. Rev. Mol. Cell Biol. **20**, 738 (2019).

[12] J. M. García-Arcos, J. Ziegler, S. Grigolon, L. Reymond, G. Shajepal, C. J. Cattin, A. Lomakin, D. Müller, V. Ruprecht, S. Wieser, R. Voituriez, and M. Piel, Advected percolation in the actomyosin cortex drives amoeboid cell motility, bioRxiv (2022).

[13] G. T. Charras, M. Coughlin, T. J. Mitchison, and L. Mahadevan, Life and times of a cellular bleb, Biophys. J. **94**, 1836 (2008).

[14] G. T. Charras, J. C. Yarrow, M. A. Horton, L. Mahadevan, and T. J. Mitchison, Non-equilibration of hydrostatic

pressure in blebbing cells, Nature (London) **435**, 365 (2005).

[15] J. Y. Tinevez, U. Schulze, G. Salbreux, J. Roensch, J. F. Joanny, and E. Paluch, Role of cortical tension in bleb growth, Proc. Natl. Acad. Sci. USA **106**, 18581 (2009).

[16] G. Charras and E. Paluch, Blebs lead the way: How to migrate without lamellipodia, Nat. Rev. Mol. Cell Biol. **9**, 730 (2008).

[17] K. Aoki, S. Harada, K. Kawaji, K. Matsuzawa, S. Uchida, and J. Ikenouchi, STIM-Orai1 signaling regulates fluidity of cytoplasm during membrane blebbing, Nat. Commun. **12**, 480 (2021).

[18] T. Zulueta-Coarasa and R. Fernandez-Gonzalez, in *Integrative Mechanobiology: Micro- and Nano- Techniques in Cell Mechanobiology*, edited by Y. Sun, D.-H. Kim, and C. A. Simmons (Cambridge University Press, Cambridge, 2015), p. 128.

[19] M. Mayer, M. Depken, J. S. Bois, F. Julicher, and S. W. Grill, Anisotropies in cortical tension reveal the physical basis of polarizing cortical flows, Nature (London) **467**, 617 (2010).

[20] L. L. Pontani, J. van der Gucht, G. Salbreux, J. Heuvingh, J. F. Joanny, and C. Sykes, Reconstitution of an actin cortex inside a liposome, Biophys. J. **96**, 192 (2009).

[21] K. Carvalho, F. C. Tsai, E. Lees, R. Voituriez, G. H. Koenderink, and C. Sykes, Cell-sized liposomes reveal how actomyosin cortical tension drives shape change, Proc. Natl. Acad. Sci. USA **110**, 16456 (2013).

[22] H. Miyata and H. Hotani, Morphological changes in liposomes caused by polymerization of encapsulated actin and spontaneous formation of actin bundles, Proc. Natl. Acad. Sci. USA **89**, 11547 (1992).

[23] H. Miyata and K. Kinosita, Jr., Transformation of actin-encapsulating liposomes induced by cytochalasin D, Biophys. J. **67**, 922 (1994).

[24] H. Miyata, S. Nishiyama, K. Akashi, and K. Kinosita, Jr., Protrusive growth from giant liposomes driven by actin polymerization, Proc. Natl. Acad. Sci. USA **96**, 2048 (1999).

[25] C. Simon, R. Kusters, V. Caorsi, A. Allard, M. Abou-Ghali, J. Manzi, A. Di Cicco, D. Levy, M. Lenz, J. F. Joanny, C. Campillo, J. Plastino, P. Sens, and C. Sykes, Actin dynamics drive cell-like membrane deformation, Nat. Phys. **15**, 602 (2019).

[26] K. Guevorkian, J. Manzi, L. L. Pontani, F. Brochard-Wyart, and C. Sykes, Mechanics of biomimetic liposomes encapsulating an actin shell, Biophys. J. **109**, 2471 (2015).

[27] R. Sakamoto, D. S. Banerjee, V. Yadav, S. Chen, M. Gardel, C. Sykes, S. Banerjee, and M. P. Murrell, Membrane tension induces F-actin reorganization and flow in a biomimetic model cortex, Commun. Biol. **6**, 325 (2023).

[28] E. Loiseau, J. A. M. Schneider, F. C. Keber, C. Pelzl, G. Massiera, G. Salbreux, and A. R. Bausch, Shape remodeling and blebbing of active cytoskeletal vesicles, Sci. Adv. **2** (2016).

[29] Y. Bashirzadeh, H. Moghimianavval, and A. P. Liu, Encapsulated actomyosin patterns drive cell-like membrane shape changes, iScience **25**, 104236 (2022).

[30] M. Murrell, L. L. Pontani, K. Guevorkian, D. Cuvelier, P. Nassoy, and C. Sykes, Spreading dynamics of biomimetic actin cortices, Biophys. J. **100**, 1400 (2011).

[31] A. F. Straight, A. Cheung, J. Limouze, I. Chen, N. J. Westwood, J. R. Sellers, and T. J. Mitchison, Dissecting temporal and spatial control of cytokinesis with a myosin II inhibitor, Science **299**, 1743 (2003).

[32] I. Linsmeier, S. Banerjee, P. W. Oakes, W. Jung, T. Kim, and M. P. Murrell, Disordered actomyosin networks are sufficient to produce cooperative and telescopic contractility, Nat. Commun. **7**, 12615 (2016).

[33] M. Schuppler, F. C. Keber, M. Kroger, and A. R. Bausch, Boundaries steer the contraction of active gels, Nat. Commun. **7**, 13120 (2016).

[34] See Supplemental Material at http://link.aps.org/supplemental/10.1103/PhysRevResearch.6.033024 for Figs. S1–S9, and Movies S1–S3.

[35] K. Carvalho, J. Lemiere, F. Faqir, J. Manzi, L. Blanchoin, J. Plastino, T. Betz, and C. Sykes, Actin polymerization or myosin contraction: Two ways to build up cortical tension for symmetry breaking, Philos. Trans. R. Soc., B **368**, 20130005 (2013).

[36] E. S. Welf, C. E. Miles, J. Huh, E. Sapoznik, J. Chi, M. K. Driscoll, T. Isogai, J. Noh, A. D. Weems, T. Pohlkamp, K. Dean, R. Fiolka, A. Mogilner, and G. Danuser, Actin-membrane release initiates cell protrusions, Dev. Cell **55**, 723 (2020).

[37] C. G. Muresan, Z. G. Sun, V. Yadav, A. P. Tabatabai, L. Lanier, J. H. Kim, T. Kim, and M. P. Murrell, F-actin architecture determines constraints on myosin thick filament motion, Nat. Commun. **13**, 7008 (2022).

[38] K. L. Weirich, S. Stam, E. Munro, and M. L. Gardel, Actin bundle architecture and mechanics regulate myosin II force generation, Biophys. J. **120**, 1957 (2021).

[39] K. Dierkes, A. Sumi, J. Solon, and G. Salbreux, Spontaneous oscillations of elastic contractile materials with turnover, Phys. Rev. Lett. **113**, 148102 (2014).

[40] R. Sakamoto, M. Tanabe, T. Hiraiwa, K. Suzuki, S. Ishiwata, Y. T. Maeda, and M. Miyazaki, Tug-of-war between actomyosin-driven antagonistic forces determines the positioning symmetry in cell-sized confinement, Nat. Commun. **11**, 3063 (2020).

[41] D. S. Banerjee, A. Munjal, T. Lecuit, and M. Rao, Actomyosin pulsation and flows in an active elastomer with turnover and network remodeling, Nat. Commun. **8**, 1121 (2017).

[42] M. Reconditi, M. Linari, L. Lucii, A. Stewart, Y. B. Sun, P. Boesecke, T. Narayanan, R. F. Fischetti, T. Irving, G. Piazzesi, M. Irving, and V. Lombardi, The myosin motor in muscle generates a smaller and slower working stroke at higher load, Nature (London) **428**, 578 (2004).

[43] G. Piazzesi, M. Reconditi, M. Linari, L. Lucii, P. Bianco, E. Brunello, V. Decostre, A. Stewart, D. B. Gore, T. C. Irving, M. Irving, and V. Lombardi, Skeletal muscle performance determined by modulation of number of myosin motors rather than motor force or stroke size, Cell **131**, 784 (2007).

[44] S. Stam, J. Alberts, M. L. Gardel, and E. Munro, Isoforms confer characteristic force generation and mechanosensation by myosin II filaments, Biophys. J. **108**, 1997 (2015).

[45] O. Wagner, J. Zinke, P. Dancker, W. Grill, and J. Bereiter-Hahn, Viscoelastic properties of f-actin, microtubules, f-actin/alpha-actinin, and f-actin/hexokinase determined in microliter volumes with a novel nondestructive method, Biophys. J. **76**, 2784 (1999).

[46] F. Nakamura, E. Osborn, P. A. Janmey, and T. P. Stossel, Comparison of filamin A-induced cross-linking and Arp2/3 complex-mediated branching on the mechanics of actin filaments, J. Biol. Chem. **277**, 9148 (2002).

[47] J. Brugues, B. Maugis, J. Casademunt, P. Nassoy, F. Amblard, and P. Sens, Dynamical organization of the cytoskeletal cortex probed by micropipette aspiration, Proc. Natl. Acad. Sci. USA **107**, 15415 (2010).

[48] S. Deshpande, S. Wunnava, D. Hueting, and C. Dekker, Membrane tension-mediated growth of liposomes, Small **15**, e1902898 (2019).

[49] C. Fang, T. H. Hui, X. Wei, X. Shao, and Y. Lin, A combined experimental and theoretical investigation on cellular blebbing, Sci. Rep. **7**, 16666 (2017).

[50] W.-h. Chou, M. Molaei, H. Wu, P. W. Oakes, J. R. Beach, and M. L. Gardel, Limiting pool and actin architecture controls myosin cluster sizes in adherent cells, Biophys. J. **123**, 157 (2024).

[51] M. A. Quintanilla, H. Patel, H. Wu, K. A. Sochacki, M. Akamatsu, J. D. Rotty, F. Korobova, J. E. Bear, J. W. Taraska, P. W. Oakes, and J. R. Beach, Local monomer levels and established filaments potentiate non-muscle myosin 2 assembly, J. Cell Biol. **223**, e202305023 (2024).

[52] M. Beck, A. Schmidt, J. Malmstroem, M. Claassen, A. Ori, A. Szymborska, F. Herzog, O. Rinner, J. Ellenberg, and R. Aebersold, The quantitative proteome of a human cell line, Mol. Syst. Biol. **7**, 549 (2011).

[53] A. Uvizl, R. Goswami, S. D. Gandhi, M. Augsburg, F. Buchholz, J. Guck, J. Mansfeld, and S. Girardo, Efficient and gentle delivery of molecules into cells with different elasticity via progressive mechanoporation, Lab Chip **21**, 2437 (2021).

[54] A. Bretscher, D. Reczek, and M. Berryman, Ezrin: A protein requiring conformational activation to link microfilaments to the plasma membrane in the assembly of cell surface structures, J. Cell Sci. **110** (Pt. 24), 3011 (1997).

[55] M. Kovács, K. Thirumurugan, P. J. Knight, and J. R. Sellers, Load-dependent mechanism of nonmuscle myosin 2, Proc. Natl. Acad. Sci. USA **104**, 9994 (2007).

[56] P. Rangamani, G. Y. Xiong, and R. Iyengar, Multiscale modeling of cell shape from the actin cytoskeleton, Prog. Mol. Biol. Transl. Sci. **123**, 143 (2014).

[57] H. Ni and G. A. Papoian, Membrane-MEDYAN: Simulating deformable vesicles containing complex cytoskeletal networks, J. Phys. Chem. B **125**, 10710 (2021).